Experimental studies on droplet formation in a flow-focusing microchannel in the presence of surfactants

Roumpea, Evangelia; Kovalchuk, Nina M.; Chinaud, Maxime; Nowak, Emilia; Simmons, Mark J.h.; Angeli, Panagiota

[Link to publication on Research at Birmingham portal](#)

Experimental studies on droplet formation in a flow-focusing microchannel in the presence of surfactants

Evangelia Roumpea[1], Nina M. Kovalchuk[2], Maxime Chinaud[1], Emilia Nowak[3], Mark J.H. Simmons[2], Panagiota Angeli[1*]

[1]ThAMeS Multiphase, Department of Chemical Engineering, University College London, Torrington Place, London, WC1E 7JE, UK

[2] School of Chemical Engineering, University of Birmingham, Edgbaston, Birmingham B15 2TT, UK

[3]Massey University, Auckland, 0745, New Zealand

Abstract

The formation of an aqueous droplet in an organic continuous phase was studied experimentally inside a flow-focusing microchannel (190 μm x 195 μm: depth x width) in the presence of surfactants. A low viscosity silicone oil (0.0046 Pa s) was used as the continuous phase and a mixture of 48% w/w water and 52% w/w glycerol was the dispersed phase. Two ionic surfactants, $C_{12}TAB$ (50 mM) and $C_{16}TAB$ (5 mM) were added in the aqueous phase, at concentrations above the CMC values. Four regimes of drop formation were identified, namely squeezing, dripping, jetting and threading, whose boundaries changed when the surfactants were present. The drop formation process and the velocity profiles in both phases in the squeezing and dripping regimes were studied in more detail using a two-colour Particle Image Velocimetry technique. For all solutions studied, three distinct drop formation stages were identified, expansion, necking and pinch-off. The surfactant-laden solutions produced smaller drops. Considering the dynamic interfacial tension, rather than the equilibrium one, it was possible to explain differences in the drop formation between the two surfactant systems in the expansion stage. The forces acting on the forming drops were estimated and showed that the drag force overcomes the interfacial tension force at the transition between the expansion and necking stages. During this transition, the curvature of the neck changes while

* corresponding author: p.angeli@ucl.ac.uk

its thinning rate was increased. The transition from the necking to the pinch-off stage was signified by a flow reversal at the bottom part of the drop.

1. Introduction

Recently emerged microfluidic approaches promise to deliver reliable production and manipulation of droplets with controlled size, which is very significant for applications such as reactions, separations, emulsifications and inkjet printing (Liu and Zhang, 2011; Seemann et al., 2012). The small characteristic dimensions of the microchannels result in portable devices, while the laminar flows and the high surface-to-volume ratios enhance the importance of surface and interfacial forces and make possible the control of the flow patterns formed. The geometry of the microfluidic channel can significantly affect droplet formation. Several inlet configurations have been proposed to enable uniform droplet size at high frequency, such as flow-focusing, T- or Y- junction and co-flowing inlets (Anna, 2016). Flow-focusing devices have been found to produce monodisperse droplets, but have been much less investigated compared to T-junction configurations (Chiarello et al., 2017; Christopher et al., 2008; Garstecki et al., 2006). In flow-focusing geometries, the resulting drop size depends on the dispersed to continuous phase flowrate ratio and the Capillary number, Ca (Fu et al., 2009) while the droplet formation process has been described by several empirical correlations (Cubaud and Mason, 2008; Fu et al., 2016). From studies in a wide range of channel geometries and sizes, fluid viscosities and interfacial tensions, four regimes of droplet formation have been identified, i.e. squeezing, dripping, jetting and threading (Cubaud and Mason, 2008; Kovalchuk et al., 2018; Lee et al., 2009). At low viscosity ratios, $\mu_d/\mu_c < 0.1$, intermediate flow rate ratios $Q_d/Q_c < 1/40$ and intermediate surfactant concentrations the tip streaming regime has also been observed in flow focusing devices, where surfactants are swept to the tip of the drop and locally reduce the interfacial tension and result in the breakage of small droplets (Anna, 2016).

Garstecki et al. (2006) studied the drop (bubble) breakup process at low Ca numbers (squeezing flow regime) in a confined T-junction geometry and reported that the drop length is proportional to the dispersed to continuous phase flow rate ratio. They observed that as the dispersed phase plug penetrates into the main channel, it blocks the continuous phase flow. This blockage leads to an increasing pressure inside the continuous phase and eventually to the squeezing of the dispersed phase. They described the droplet formation in the squeezing regime by considering three main forces: the interfacial tension force resisting the break-up, the shear stress acting on the forming droplet by the continuous phase and the squeezing pressure across the droplet. Christopher et al. (2008) and Glawdel et al. (2012b) used a similar force balance to estimate the magnitude of the shear and the pressure forces and predicted the filling volume, neck curvature and frequency of the drops formed in a T-junction channel. Timgren et al. (2008) who studied the formation of an organic phase droplet in an aqueous continuous phase inside a rectangular T-junction channel (width of the dispersed phase inlet << width of the continuous phase inlet) considered that drag, lift, inertial, buoyancy and interfacial forces act during drop detachment. Recently, Chen et al. (2015) developed a physical model to describe the droplet formation in the squeezing regime, considering the 3D curved interface of the forming drop. Assuming that the mass of both the dispersed and the continuous phases is conserved and based on the pressure-driven squeezing mechanism proposed by Garstecki et al. (2005), they modelled the shape of the droplet during a formation cycle. In the dripping regime, the dynamics of the formation are found to be mainly governed by the interfacial tension and the shear forces. The surface tension force initially dominates but the shear forces eventually become comparable and exceed the surface tension force leading to drop detachment (Utada et al., 2007; Wang et al., 2009).

Despite the work in the literature, the knowledge of the hydrodynamics inside and outside the droplet during formation is still rather limited, especially when surface active agents are

present. Surfactants are usually added either to the continuous or the dispersed phase to enhance drop stability. They add, however, complexity in the system since they can induce interfacial tension gradients (Marangoni effects) and alter the dynamics of droplet breakup (Wang et al., 2009). Graaf et al. (2006) conducted experiments in a T-junction device using hexadecane as the dispersed phase and surfactant aqueous solutions as the continuous phase. They found that higher surfactant concentrations lead to smaller droplets and shorter droplet formation times. The formation of water/glycerol droplet in an organic continuous phase in the presence of surfactants was studied by Glawdel and Ren (2012) at a T-junction. By analysing the changes in the droplet surface area with high speed imaging, they estimated the dynamic interfacial tension. We need the drop formation process as a function of the surfactant properties and the experimental conditions. Kovalchuk et al. (2016) studied experimentally how the kinetics of thinning of liquid bridges during the breakage of surfactant-laden drops (using $C_{10}TAB$, $C_{12}TAB$, $C_{16}TAB$, SLES, Triton X-100) are affected by both the surfactant activity and concertation. They found that the less active surfactants (with high critical micelle concentration, CMC) behave like pure liquids with constant interfacial tension value. When more active surfactants were used (low CMC values), the kinetics of the neck thinning close to the pinch-off were found to depend mainly on the dynamics of adsorption of the surfactant to the drop neck.

For a better understanding of the drop formation process, knowledge of the velocity fields in the continuous and dispersed phases would be necessary to evaluate the effects of surfactants. Micro Particle Image Velocimetry (micro-PIV, μPIV) techniques have been extensively used to obtain velocity fields in microchannels. Steijn et al. (2007) studied the formation of bubbles in a T-junction microchannel using a micro-PIV system and constructed three-dimensional velocity fields in the continuous phase from measurements at different channel depths. Funfschilling et al. (2009) measured with μPIV the velocity fields in aqueous

solutions of SDS around oil droplets as they were forming in a flow focusing microchannel device in the dripping regime. The velocity data revealed that immediately after drop detachment, there is a stagnation point between the newly formed drop that moves towards the main channel and the dispersed phase interface that pulls back into the dispersed phase channel. This stagnation point is found to be driven by the interfacial tension and alters the local flow fields in the cross-junction inlet. Fu et al. (2012) also examined the velocity field in a water/glycerol continuous phase surrounding an oil drop forming in a flow-focusing device. For low viscosity ratios (μ_{Oil}/μ_{Water}, where μ is the viscosity) the droplet size was found to scale with the flow rate ratio of the phases (Q_{Oil}/Q_{Water}, where Q is the flowrate) and the Ca number of the continuous phase ($0.002 < Ca < 0.11$) whereas for high viscosity ratios it was correlated with the continuous phase Weber number ($0.015 < We < 0.44$).

The present work aims to improve the understanding of the droplet formation process in a flow-focusing device when surfactants are present. In a previous work (Kovalchuk et al., 2018) it was found that surfactants C12TAB and C16TAB only affect the drop formation patterns at concentrations above their CMC values. In the current paper these surfactants are used at concentrations 50 mM for $C_{12}TAB$ and 5 mM for $C_{16}TAB$, where they have the same equilibrium interfacial tension but different absorption kinetics. To investigate the effect of the different kinetics on the drop formation process and on the final drop size, a novel two-colour micro-PIV technique is used to obtain detailed hydrodynamic properties and velocity fields in both phases. Differences between the two surfactant systems were only found in the initial drop expansion stage. A mechanistic model is developed, based on the hydrodynamic data, to describe the evolution of the forces acting at the drop at the various formation stages.

2. Materials, experimental method and data processing

2.1 Materials

All experiments were conducted with a low viscosity silicone oil (0.0046 Pa s, Sigma-Aldrich) as the continuous phase and a mixture of 48% w/w water and 52% w/w glycerol as the dispersed phase. The aqueous phase was selected to match the refractive index of the oil (n_D^{20} = 1.39) and to eliminate any light refractions and optical distortions during the PIV measurements. Two ionic surfactants, dodecyltrimethylammonium bromide ($C_{12}TAB$), (Across organics, 99 %, M_W = 308 g/mol) and hexadecyltrimethylammonium bromide ($C_{16}TAB$), (Sigma, BioXtra, $\geq$ 99 %, M_W = 364 g/mol) were tested. The surfactants were dissolved in the aqueous phase and one concentration of each surfactant was used in the current experiments: 50 mM for $C_{12}TAB$ and 5 mM for $C_{16}TAB$. The interfacial tension isotherms for $C_{12}TAB$ and $C_{16}TAB$ surfactant solutions are presented in **Figure 1**. In both cases, the concentrations are higher than the CMC values which are ~ 20 mM and ~2 mM for $C_{12}TAB$ and $C_{16}TAB$ respectively. Concentrations above CMC were chosen to ensure that an adequate surfactant concentration will be adsorbed on any newly formed interface (Funfschilling et al., 2009). In addition, in a previous work with the same surfactants (Kovalchuk et al., 2018) it was found that low surfactant concentrations did not affect the flow pattern map significantly. For this reason, surfactant concentrations above the CMC values were chosen which have a more pronounced effect on the flow pattern map. The two concentrations (50 mM for $C_{12}TAB$ and 5 mM for $C_{16}TAB$) were selected because at equilibrium they result in systems with similar interfacial tension; these two surfactants, however, have different absorption kinetics during the droplet formation process (Kovalchuk et al., 2018).
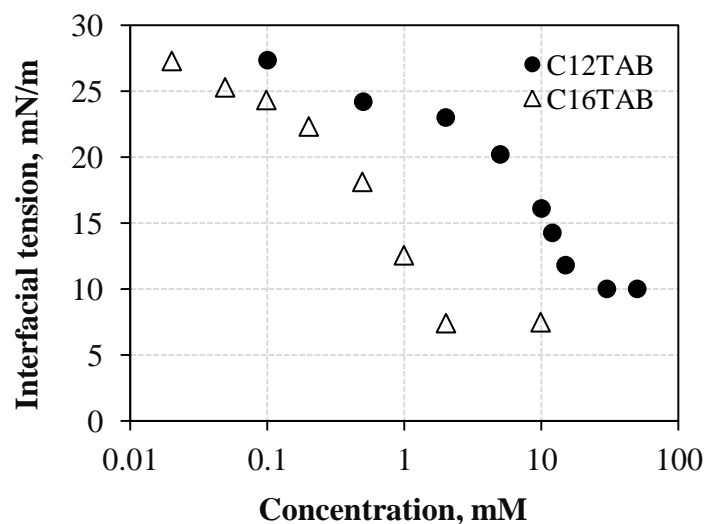
6

Figure 1: Equilibrium interfacial tension against concentration for the surfactants C_{12}TAB and C_{16}TAB.

In **Table 1** the properties of the liquids used are summarized. The equilibrium interfacial tension for the oil and the surfactant solutions was measured using the Du Noüy ring method (K100 KRUSS GmbH®). The viscosity of each solution was measured with an Advanced Rheometric Expansion System (ARES, TA Instruments®); all solutions are Newtonian. As there are no suitable methods to measure the dynamic interfacial tension on the time scales of the droplet formation in microchannels (the drop formation time in the present study is below 1s), the dynamic surface tension (liquid/air interface) was used to indicate trends for the dynamic interfacial tension. The dynamic surface tension was measured using the maximum bubble pressure tensiometer technique which can provide results in millisecond time scales (Kovalchuk et al., 2018). It was found that at short times the C16TAB system (CMC = 5 mM) has high surface tension (close to the surfactant-free system), whereas at long times it has low surface tension (close to the C12TAB system). The C12TAB system (CMC = 50 mM) was found to equilibrate much faster having similar surface tension values at both short and long times. The difference on the absorption rates of the two surfactants at the surfaces

7

was attributed to the lower CMC values of the C16TAB system compared to the C12TAB system.

Table 1: Properties of the test fluids (T = 20°C).

Fluid system			ρ, (kg/m^3)	μ, Pa s	σ_{eq}.*, (mN/m)
Dispersed phase	Surfactant-free	Aqueous glycerol solution (52% w/w)	1142	0.007	29
	C_{12}TAB	Aqueous glycerol solution (52% w/w)+ 50 mM	1142	0.007	10
	C_{16}TAB	Aqueous glycerol solution (52% w/w) + 5mM	1142	0.007	7.3
Continuous phase	O	Silicone oil	920	0.0046	-

*equilibrium interfacial tension

2.2 Experimental methods

The experimental setup employed in the drop formation study is presented in **Figure 2**. The experiments were conducted in a glass flow-focusing device with cross-junction equal to 190 μm x 195 μm (depth x width) and channels equal to 190 μm x 390 μm (Dolomite® microfluidics). Two syringe pumps (KDS Scientific®) were used to feed separately the two phases into the test section. The aqueous surfactant solutions (dispersed phase) were injected into the central channel whereas the silicone oil (continuous phase) was pumped via the two side channels. For each set of runs, the aqueous phase flow rate was kept constant and the organic phase flowrate was increased stepwise. The aqueous phase flow rates ranged from 0.01 to 0.1 cm^3/min, whereas the organic phase flow rates varied from 0.003 to 0.1 cm^3/min.

A two-colour micro-PIV system (TSI Inc.), as presented in **Figure 2,** was used to obtain the flow regimes and the velocity profiles in the two phases (for details see Chinaud et al. (2015)). The aqueous phase was seeded with 1 μm carboxylate-modified microspheres FluoSpheres® (540/560 nm) and the organic phase with 1 μm blue silica microspheres particles Sicastar® (350/440 nm). Rhodamine 6G fluorescent dye (1 ppm) was also added in

8

the aqueous phase to improve the detection of the liquid-liquid interface. Illumination was provided by a double pulsed Nd:YAG laser (Litron Lasers®) which emits simultaneously two different wavelengths, blue and green (355 and 532 nm). The light was guided with an optical fibre to the test section placed at an inverted microscope (Nikon Eclipse Ti-s) with a 10x magnification. The light emitted from the seeded fluids in the test section was directed from the microscope to a beam splitter (Andor® Technology) where the orange light (560 nm), emitted by the aqueous phase, was led through a dichroic mirror and a high-pass filter to a 4MP, 32fps, CCD camera Link® Base (TSI, Powerview 4MP, with 2048×2048 pixels resolution and 2x magnification lens).
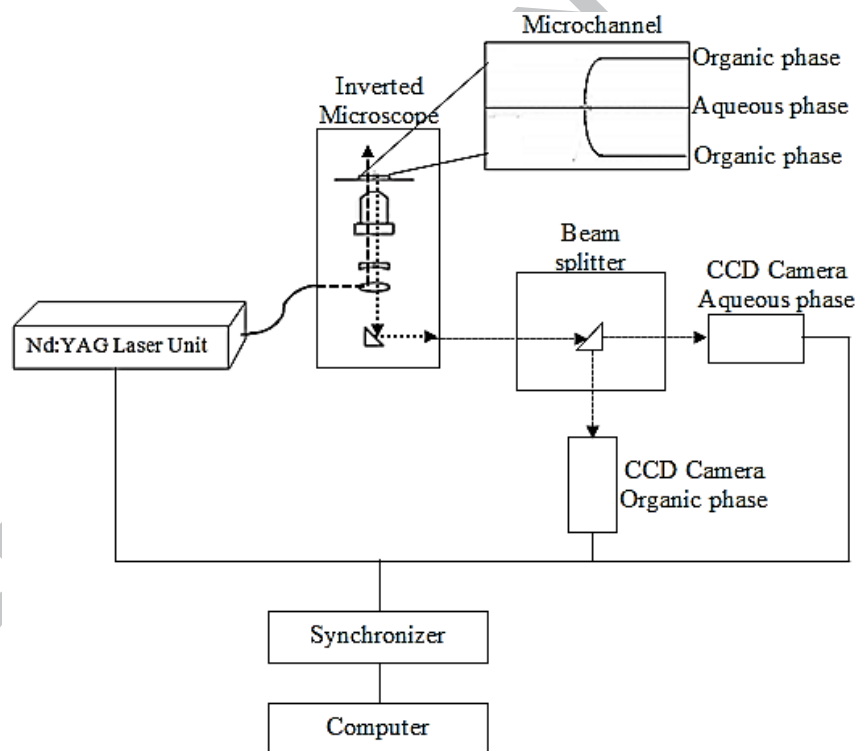
Figure 2: Schematic of the experimental setup.

The blue light (440 nm), emitted by the organic phase, was reflected by the dichroic mirror and was led through a band pass filter to a 12-bit CCD camera Dicam pro® (PCO Sensicam, Dicam pro® with 1270×512 pixels resolution and 1x magnification lens). Both cameras were connected to a laser pulse synchronizer (TSI Inc.) and a PC. The PIV acquisition frequency was 7 Hz per image pair. The μPIV measurement depth for the blue (355 nm) and green (532

nm) wavelengths was approximately 20 μm and 26 μm (~10% of the channel depth at the cross-junction) respectively, using a microscope lens with magnification equal to 10x (NA = 0.30, n=1). It was found that neither the fluorescent dye nor the tracer particles affected the properties of the phases or the equilibrium interfacial tension values.

2.3 PIV data processing

A PIV image processing software (Insight 4G, TSIInc.) and MATLAB R2014a codes developed in-house were used for image treatment, detection of the liquid-liquid interface and calculation of average velocity fields in the two phases. For both cameras, a primary-to-secondary correlation peak ratio was used to remove the false vectors whereas any vectors outside the seeded phases were set to zero. The PIV correlation box size for the CCD camera recording the aqueous phase was set to 64×64 pixels with 50% spatial overlapping which results in a final spatial resolution of 11.9×11.9 μm. For the camera recording the organic phase, the interrogation area was set to 128×64 pixels, without overlapping, leading to a spatial resolution of 132.8×66.4 μm and a clear displacement of the organic phase vectors. For the computation of the velocity fields a recursive Nyquist grid with an FFT correlation calculation was used and the two-component velocity field was reconstructed within the Eulerian frame of reference. Based on the optical parameters of the setup, the effective particle diameter, d_e, was found to be 25 μm for the carboxylate-modified fluorescent particles and 20 μm for the silicaparticles providing an uncertainty equal to $d_e/10M = 0.25$μm for the aqueous phase and $d_e/10M = 0.20$μm for the organic phase.

A 7×7 pixels computation median filter was applied to the PIV images in MATLAB. From the mean intensity of the pictures, a threshold value was found which was used to binarize the aqueous phase images and reconstruct the interface by fitting the contour of the white region. The same process was also applied to the organic phase images. To match the velocity fields of the two phases in the same frame, the contours of the reconstructed interfaces of both the

aqueous and the organic phase images were used as an adaptive mask for the image of each camera. For each experiment, the time delay between the two laser cavities was adjusted from 40 μs to 3000 μs (depending on the flow rate of both phases) so that the maximum particle displacement would not exceed half of the final correlation box size. Image pairs were recorded during the droplet formation process. Since the acquisition frequency of the system is low (7 Hz), the drop formation process could not be resolved in time; instead image pairs were acquired at different drop *propagation steps* using as reference the droplet tip position in the channel. Each propagation step refers, therefore, to a particular tip position in the channel. To calculate averaged velocity fields, 600 micro-PIV images were obtained in each run. Depending on the flow rates, about 30 to 50 of the images were averaged to obtain the velocity fields at each drop propagation step.

3. Experimental observations and discussion

3.1 Flow pattern map

Under the current experimental conditions, different flow regimes namely squeezing, dripping, jetting and threading were observed in the cross-junction device. **Figure 3** presents the flow pattern map for the surfactant-free solution based on the volumetric flow rate of each phase, together with representative images of the corresponding patterns. The flow pattern map is in good agreement with the results obtained by Kovalchuk et al. (2018) in a similar system, which confirms that the added tracers and dye do not affect the flows. In the literature, Ca numbers are often used to represent the droplet formation regimes. In the current study the Ca numbers of the continuous $Ca_c = \frac{\mu_c \cdot Q_c}{\sigma \cdot A_{cross}}$ and dispersed phases, $Ca_d = \frac{\mu_d \cdot Q_d}{\sigma \cdot A_{cross}}$ vary only with the flowrates of fluids and the interfacial tension (μ_c, Q_c and μ_d, Q_d are the viscosities and flowrates of the continuous and dispersed phases respectively, σ is the interfacial tension, and A_{cross} is the cross-sectional area of the channel). The dynamic interfacial tension values are not known, while, as will be discussed below, the dynamic

11

phenomena seem to be relevant in the very first stages of drop formation and at later stages equilibrium values establish. If equilibrium interfacial tension values are used, then Ca depends only on the phase flow rates and these are used in **Figure 3**. By using this representation the differences between the various systems were also shown more clearly.
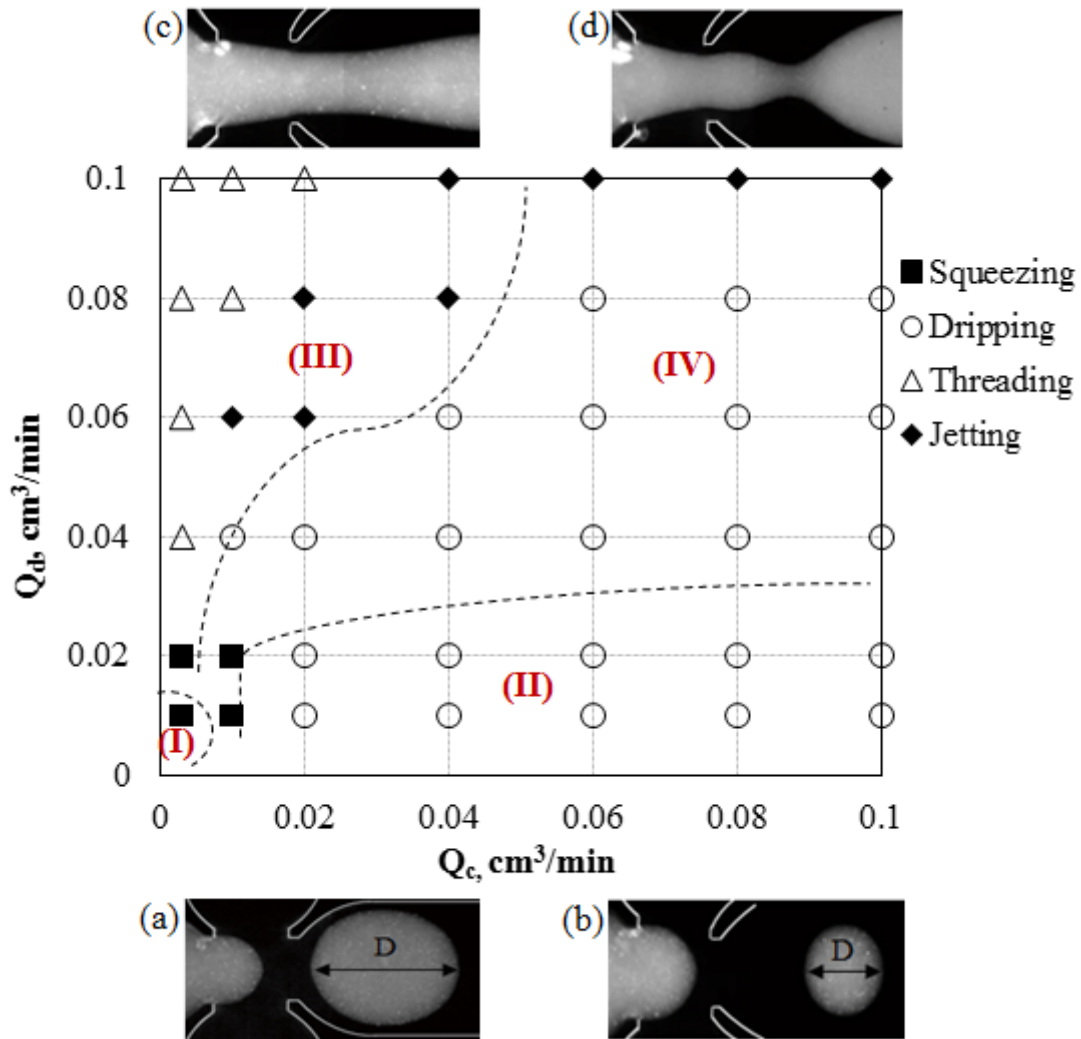

Figure 3: Flow pattern map of the surfactant-free solution and theC_{12}TAB solution and the silicone oil. Representative flow patterns (a) Plug flow (b) Drop flow (c) Thread flow (d) Jet flow. The dashed lines show the flow regime boundaries when the C_{12}TAB solution is used. Roman numbers indicate regimes in the system with surfactant (I) Squeezing regime (II) Dripping regime (III) Threading regime and (IV) Jetting regime. D is the droplet size plugs immediately after the break-up inside the cross-junction inlet.

The squeezing regime (■), occurred at low flow rates 0.003 cm^3/min < Q_d < 0.03 cm^3/min and 0.003 cm^3/min < Q_c < 0.01 cm^3/min. In this regime, the breakup of the plug (**Figure 3a)** is dominated by the excessive pressure that builds up in the continuous phase during the plug formation. As the plug is forming, it obstructs the cross-junction and restricts the flow of the continuous phase to a thin film on the channel walls. As a result, the pressure inside the continuous phase increases and 'squeezes' the plug neck (Garstecki et al., 2006). The length of the plugs was found to be greater than the main channel width (L_P> 390 μm), while a thin film of the continuous phase separated the plugs from the channel wall.

As the continuous phase flowrate increased, under constant Q_d, the dripping regime (○) dominates inside the microchannel. In the dripping flow pattern (**Figure 3b**), the drop formation process is controlled by the balance of viscous shear and interfacial forces (Wang et al., 2009). The forming drops do not obstruct completely the flow of the incoming continuous phase and their lengths are smaller (L_D<390 μm) than the main channel width. At low continuous phase flowrates (0.003 cm^3/min<Q_c< 0.01 cm^3/min), as the dispersed phase flowrate increased, there is a transition from the squeezing to the threading (△) regime. In the threading regime, a stable thread of the dispersed phase (**Figure 3c**) is produced in the flow-focusing inlet. The thread width was found to increase with increasing dispersed phase flow rate (for constant Q_c). An increase of the continuous phase flowrate resulted in a transition from the threading to the jetting regime (♦). In this regime, the dispersed phase is mainly driven by the drag force from the continuous phase flow that pulls it downstream and the jet becomes destabilized (**Figure 3d**). Utada et al. (2007) who studied the transition from the dripping to the jetting regime in co-flowing liquids, noticed that at large dispersed phase flowrates, the inertia force of the dispersed phase becomes comparable and acts cooperatively with the drag force from the continuous phase, shifting the pinch-off point of the drop further downstream the main channel. Kovalchuk et al. (2018) found a similar shift of the pinch-off

13

point with increasing dispersed to continuous phase flowrate ratio and noted that the length of the jet also depended on the interfacial tension i.e. the jet length increases with decreasing interfacial tension.

When the 50 mM C_{12}TAB solution was used, the boundaries shifted as shown in **Figure 3** with dashed lines. In particular, the squeezing regime and consequently plug flow was observed only in area **(I)** limited to low flow rates of both phases. The dripping regime was also reduced in the map in area **(II)** and drops were produced at low dispersed phase flowrates only (0.003 cm^3/min $< Q_d <$ 0.02 cm^3/min). However, the areas occupied by the threading and jetting regimes in the map increased. The thread flow pattern occurred for an extended range of continuous phase flowrates, 0.003 cm^3/min$< Q_c <$ 0.05 cm^3/min and for most of the dispersed phase flowrates (map area **(III)**). The jetting regime covered a large area in the map (area **(IV)**). The boundaries between regimes for the 5 mM C_{16}TAB solution, which is less concentrated than the C_{12}TAB, were in between those of the surfactant-free and of the C_{12}TAB solutions, and are not presented here. The shift in the boundaries between the regimes reveals the effect of the surfactant concentration on the drop formation process.

Droplet devices usually operate in the squeezing and dripping regimes where monodisperse droplets are generated (Xu et al., 2008). The mechanism of droplet generation in the squeezing and dripping regimes was further studied with the two-colour PIV system in the channel cross-junction.

3.2 Formation process and droplet characteristics

Following the pressure-driven mechanism proposed by Garstecki et al. (2006), **Figure 4** presents the formation process of a typical plug in the squeezing regime, which is divided into 3 stages, namely expansion, necking and pinch-off. The plug formation depends on the competition between the drag (shear stress and pressure gradient) force from the continuous phase and the interfacial tension force. At the first *expansion* stage, the dispersed phase is

expanding into the main channel (**Figure 4a**). Immediately after the pinch-off of the previous plug, the dispersed phase pulls back slightly into the dispersed phase channel inlet due to surface tension before it moves forward again into the main channel. At this initial stage, the plug grows mainly in the radial direction and slightly in the axial direction in the junction (**Figure 4a).**
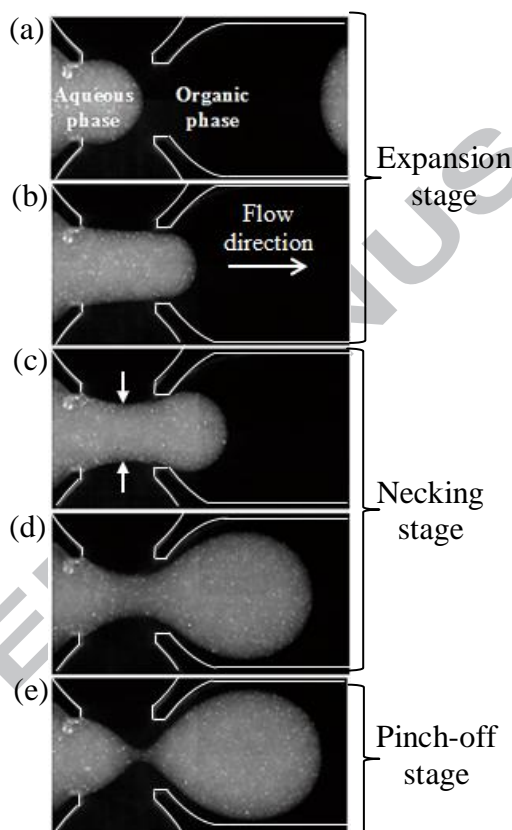

Figure 4: Typical plug formation in the flow-focusing geometry: (a) - (b) expansion stage, (c) – (d) necking stage, (e) pinch-off stage. Images obtained with the two-colour PIV system for $Q_d = Q_c = 0.01$ cm^3/min. Channel walls have been added for clarity.

Later on, the interface starts to expand in the axial direction towards the main channel. The plug reaches the edge of the main channel but it is still separated from the wall by a thin film of the continuous phase (**Figure 4b**). At this stage, the plug blocks the side inlet channels of the continuous phase, and the pressure there increases. The increased pressure overcomes the interfacial tension force and causes a change in the interface curvature and the thinning of the neck (**Figure 4c**). As neck is defined the part of the fluid that connects the dispersed phase

15

inlet with the forming droplet. The change in curvature signifies the beginning of the *necking* stage (**Figure 4c – d)** with the neck width decreasing as the dispersed phase propagates into the main channel. This change in interface curvature during drop formation has also been observed in T-junction inlets by Glawdel et al. (2012a) and Chinaud et al. (2015). During the necking stage, the flow of the continuous phase reduces the neck width in the radial direction and pushes the droplet in the axial direction. The transition between the *necking* and the *pinch off* stages was found to take place at neck widths of about 60-70 μm (depending on the continuous phase flowrate). At these neck widths a flow reversal was observed at the lower part of the drop (as revealed by the PIV results) which was used as a criterion of the transition. In addition, at this neck width the dispersed phase acquired larger velocity values at the top part of the droplet compared to the corresponding velocities at the expansion and necking stages. After the break-up, the new plug is pushed downstream in the main channel by the continuous phase and the formation process starts again. After the break-up, the new plug is pushed downstream by the continuous phase and the formation process starts again.

The same three stages of formation (expansion, necking, pinch-off stage) were also identified for the dripping regime. During the expansion stage, the interfacial tension force that acts on the forming drop initially dominates and controls the growth rate. As the droplet grows into the main channel, the shear stress inside the continuous phase increases and exceeds the interfacial tension force, thinning the neck (necking stage). In addition, the pressure inside the continuous phase increases, because its flow is restricted by the droplet. The pressure that builds up in the continuous phase is less in the dripping regime than in the squeezing regime as the growing droplet has smaller size and blocks less the area of the side channels (**Figures 3a,b**). The neck of the dispersed phase eventually breaks (pinch-off stage) and a new droplet is formed.

The thinning rate of the neck is mainly dependent on the continuous phase flowrate (Fu et al., 2009). The neck width was measured at both the expansion and the necking stages, to determine which propagation stage determines the droplet size. **Figure 5** shows the effect of the continuous phase flowrate (Q_c = 0.003–0.1 cm³/min) on the neck width, W_d, at the expansion stage just before the next, necking stage (**Figure 5, Inset**). For a constant dispersed phase flowrate (Q_d = 0.01 cm³/min) and low continuous phase flowrate (Q_c = 0.003 cm³/min) the surfactant-laden solutions give similar neck width.
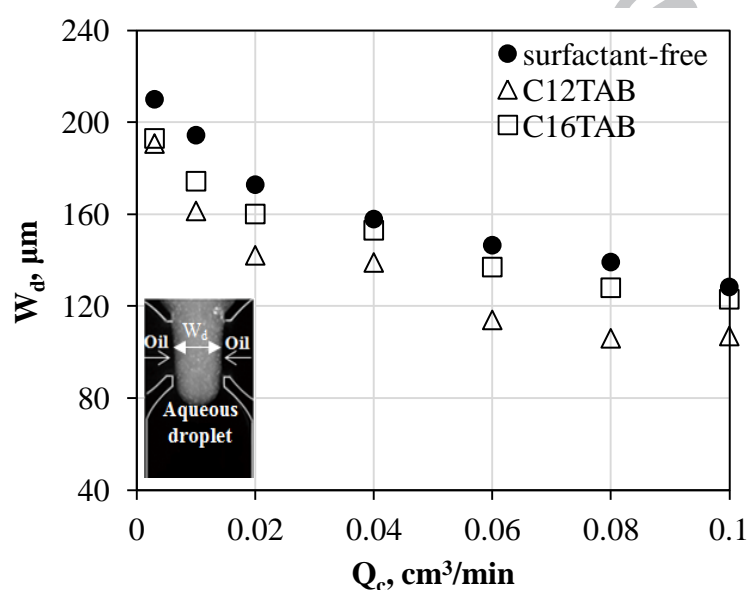

Figure 5: Effect of the continuous phase flowrate on the neck width for all the aqueous solutions used at the end of expansion stage. Q_d = 0.01 cm³/min. Inset: Neck width at the end of expansion stage.

However, with increasing Q_c, the differences in the width between the surfactant-laden solutions are becoming more pronounced. This is attributed to the differences in absorption kinetics of the two surfactants during drop formation (Baret et al., 2009; Jin et al., 2006). As was mentioned above, C16TAB appears to be reaching equilibrium at a lower rate compared to C12TAB (see also Kovalchuk et al. (2018)). When the continuous phase flowrates are high (Q_c > 0.02 cm³/min) the drop *expansion* stage is very short (in the time scale of 0.004 – 0.02 s, depending on the continuous phase flowrate, as revealed from the measurements) and the

17

concentration of C16TAB does not manage to reach equilibrium at the interface; the results (neck width) then are similar to the surfactant free system (Figure 5). This is not the case for C12TAB which absorbs faster and has time to reach equilibrium. In contrast, at low flowrates ($Q_c \leq 0.02$ cm^3/min), the expansion stage takes longer (in the time scales of $0.05 - 0.09$ s) and the concentration of C16TAB at the interface reaches a value closer to the equilibrium one. The results on neck width are in this case similar to C12TAB (**Figure 5**). The same trend was also observed for $Q_d = 0.02$ cm^3/min.

Different trends are, observed in the necking stage, as can be seen in **Figure 6**, where the neck width is plotted against the continuous phase flowrate. The data represent the minimum neck width that can be measured at the end of the necking stage.
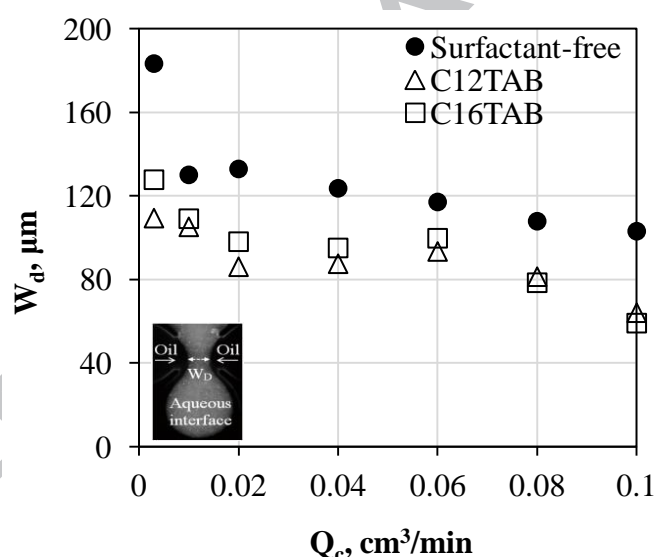

Figure 6: Effect of the continuous phase flowrate on the minimum neck width for all the aqueous solutions used at the necking stage. $Q_d = 0.01$ cm^3/min. Inset: Neck width at the necking stage.

The *necking* stage takes longer (time scales of necking stage: 0.13 s-0.58 s based on the continuous phase flowrate) and even C16TAB has time to reach the equilibrium concentration at the interface. The equilibrium interfacial tension of C16TAB is similar to C12TAB at the concentrations used, and as a result the neck widths from the two surfactants are similar at the necking stage (**Figure 6**).

18

The final drop sizes obtained for all fluid systems are shown in **Figure 7** for constant $Q_d =$ 0.01 cm^3/min. As can be seen, the two surfactant systems give similar final drop sizes (maximum deviation 8%), which are smaller than those obtained in the pure system by ~ 100 μm. The data shown in **Figure 7** correspond to the axial drop diameter, D, measured immediately after the droplet formation at the cross-junction inlet (see Inset, **Figure 7**).

Figures 6 and 7 demonstrate that the necking stage affects the final drop size more than the expansion stage. The dependence of the final droplet size on the necking stage has also been reported by Chen et al. (2015) and by Glawdel et al. (2012a). From **Figure 7** it can be seen that as Q_c increases the final drop sizes decrease for all three solutions in agreement with the findings by Wong et al. (2017) and Fu et al. (2016).
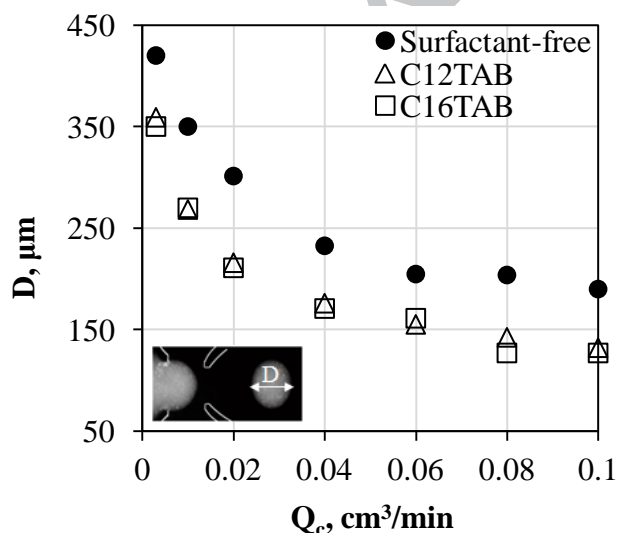

Figure 7: Final droplet axial diameter plotted against the continuous phase flowrate for all the aqueous solutionsused. Qd = 0.01 cm^3/min. Inset: Axial droplet diameter.

With increasing continuous phase flowrate, both the pressure on the side inlet continuous phase channels and the shearing effects along the interface increase and favour the thinning of the neck. As a result, the drop formation time decreases and smaller droplets are produced. At low continuous phase flowrates (0.003 cm^3/min to 0.01 cm^3/min) the droplet diameter decreases linearly with Q_c. At high continuous phase flowrates (above 0.02 cm^3/min) though,

19

the relation between the droplet diameter and the Q_c is not linear any more indicating that the formation mechanism changed from the squeezing to the dripping regime.

The changes in the neck width during the expansion and necking stages are presented in **Figure 8** for the surfactant-free and the $C_{12}TAB$ solution for all the continuous phase flow rates tested. To compare the results, the measurements were taken for the same position of the tip of the droplet; these represent different steps of the drop formation process. The last neck width point shown for each flow rate corresponds to the pinch-off stage.

Generally, the neck width decreases with time and with increasing continuous phase flow rate. The decrease of the neck width at the different steps can be divided in two linear regimes, as shown with the dashed lines (I) and (II) for $Q_c = 0.04$ cm^3/min in **Figure 8a**. These two lines represent the thinning rate of the neck, while the change in slope corresponds to the transition from the expansion to the necking stage, where the neck curvature also changes. Similar observations on the different neck width regimes have been made by Glawdel et al. (2012a) and Garstecki et al. (2005). The critical width at the transition between the two regimes is found to be below 100 μm (< channel depth/2) for most of the cases studied, apart from the lowest continuous phase flow rate, $Q_c = 0.003$ cm^3/min, where the necking stage starts after 170 μm and 150 μm neck width for the surfactant-free and the $C_{12}TAB$ solutions respectively. As the continuous phase flow rate increases, the change in slope from the expansion to the necking stage starts at an earlier propagation step for the $C_{12}TAB$ solution (**Figure 8b)** compared to the surfactant-free solution. The neck width data for $C_{16}TAB$ fall in between those of the surfactant-free and the $C_{12}TAB$ solutions and are not presented here.
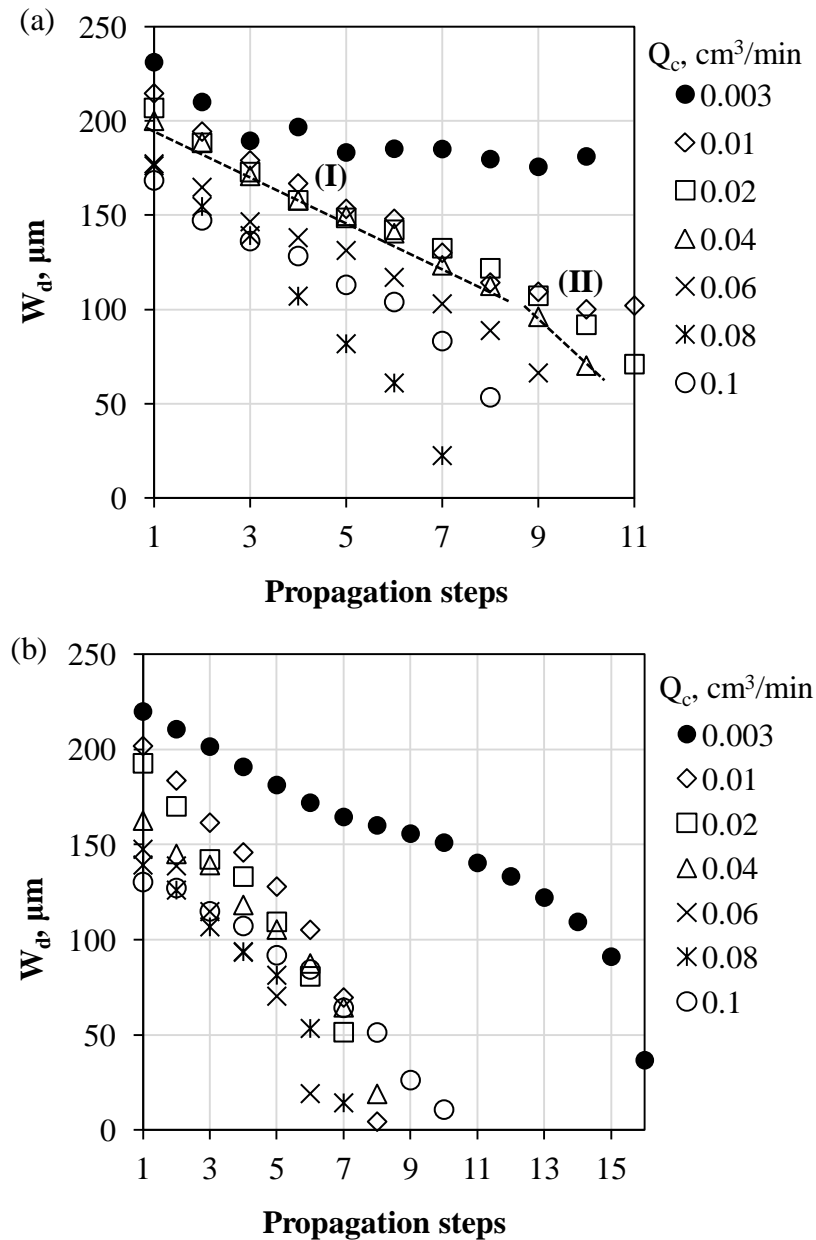
Figure 8: (a) Surfactant-free and (b) C_{12}TAB neck width as a function of the propagation steps for all the continuous phase flowrates studied. $Q_d = 0.01$ cm^3/min. The dashed lines (I), (II) have been fitted to the data for $Q_c = 0.04$cm^3/min.

The interfacial tension is found to affect the curvature of the droplet leading edge which is mainly controlled by the Laplace pressure (Glawdel and Ren, 2012). The leading edge radius was obtained from the μPIV images and is defined as the radius R of a circle fitted to the forming drop tip (**Figure 9a, Inset**). The curvature of the tip increases (radius decreases) with increasing continuous phase flow rate both at the expansion stage (**Figure 9a**) and at the

21

necking stage (**Figure 9b**). Similar to **Figures 5** and **6** for the neck width, the front radius of the $C_{16}TAB$ droplet is close to the pure system one for the expansion stage (**Figure 9a**) and to the $C_{12}TAB$ for the necking stage (**Figure 9b**). In general, for the same continuous phase flow rates, the tip radius of the surfactant-laden solutions is smaller than that of the surfactant-free system, because of the lower surface tension. Generally, during droplet formation, the tip radius increases as the droplet grows into the main channel.
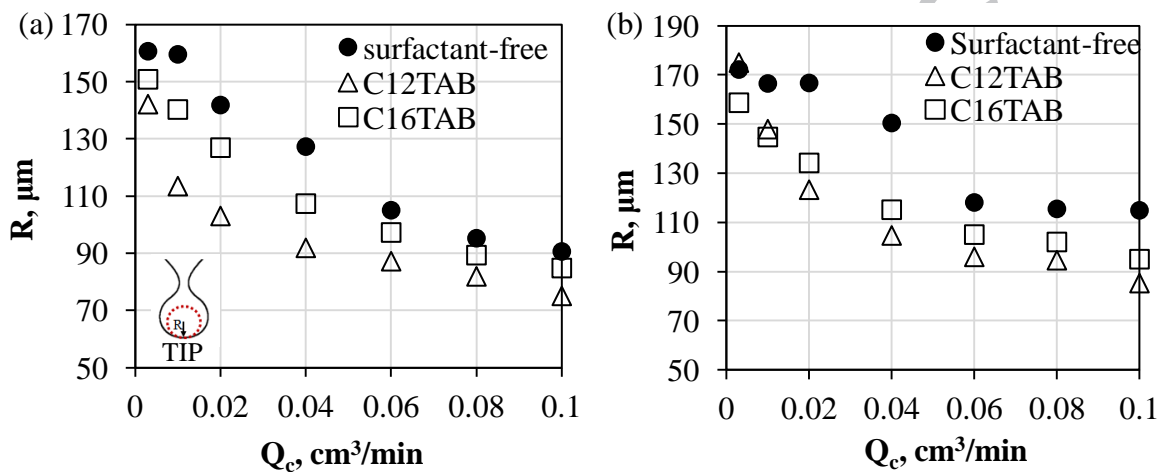

Figure 9: Effect of the continuous phase flowrate on the front radius of the forming drop at the (a) end of the expansion and (b) end of the necking stage. $Q_d = 0.01$ cm^3/min. Inset: Front radius of the droplet.

4. Force balance and velocity fields during drop formation

4.1 Forces on a droplet forming in the dripping regime

The droplet formation in the flow-focusing device is considered to be dominated by the balance between the interfacial tension force that acts against the detachment of the droplet and the drag force by the continuous phase, which pulls the droplet downstream. The formation of the neck starts once the drag force becomes sufficiently large and exceeds the interfacial tension force. **Figure 10** illustrates the forces that act on the droplet in the flow direction (y-direction) at the necking stage. The shear stress and the pressure gradient arising in the continuous phase as the droplet grows into the main channel, lead to a drag force, F_D that promotes the drop detachment.
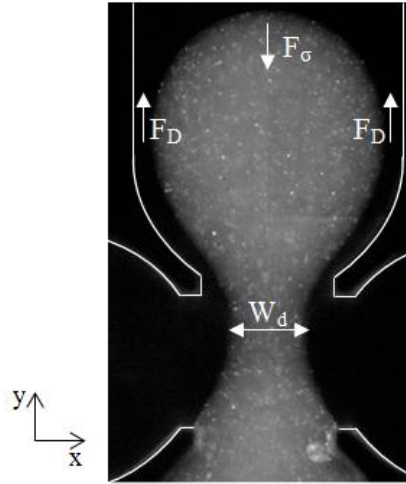
22

Figure 10: Schematic indicating the drag force (F_D) and the interfacial tension force($F\sigma$) during the necking stage.

The drag force applied by the continuous phase on the droplet acts in the positive y-direction and is defined as (Husny and Cooper-White, 2006):

$$F_D = 4\pi \cdot \mu_c \cdot \frac{(2n+3)}{(n+1)} \cdot D_d \cdot (u_c^* - u_d) \tag{1}$$

where μ_c is the continuous phase viscosity, n is the viscosity ratio between the two phases $n = \mu_c / \mu_d$, D_d is the droplet diameter and $(u_c^* - u_d)$ is the relative local velocity between the continuous phase, $u_c^* = 2 \cdot u_c \cdot \left[1 - \frac{D_c - D_d}{D_c}\right]$ (where D_c is the hydraulic diameter of the continuous phase channel and u_c is the continuous phase velocity) and the droplet velocity, u_d.

The interfacial tension force acts in the negative direction of the flow opposing the drop detachment. The interfacial tension force acting on the droplet is found from the Laplace pressure difference on the drop surface and is given by:

$$F_\sigma = \sigma \cdot \left(\frac{1}{R} + \frac{2}{h}\right) \cdot \left(\pi \cdot \frac{W_d^2}{4}\right) \tag{2}$$

where σ is the interfacial tension, R is the leading edge radius of the drop, h is the depth of the channel and W_d is the neck width (**Figure 10**). For the surfactant-free system, the interfacial tension σ is constant and equal to 29 mN/m. The interfacial tension of the C_{12}TAB solution will be assumed to be constant and equal to the equilibrium value, $\sigma = 10$ mN/m, for

23

all the formation stages. This assumption is based on the work of Kovalchuk et al. (2018) who found that the dynamic surface tension of $C_{12}TAB$ surfactant reaches the equilibrium value very fast. The use of the equilibrium value is further justified given the approximate nature of the model which considers forces acting on the whole drop following similar approaches in the literature (Christopher et al., 2008; Glawdel et al., 2012b; Husny and Cooper-White, 2006), as well as the lack of knowledge of dynamic interfacial tension.

These forces will be further used to explain the droplet formation in the flow-focusing microchannel along with the velocities obtained with the PIV.

4.2 Velocity fields inside and outside a forming droplet in the dripping regime

The images and the velocity fields obtained from the two-colour PIV measurements can reveal how the surfactants alter the drop formation process and the flow fields inside and outside the droplet. **Figure 11** and **Figure 12** show the averaged total velocity fields at 4 different steps during the drop formation process of the surfactant-free and the surfactant-laden 50 mM $C_{12}TAB$ solutions respectively for the same continuous and dispersed phase flowrates.

In the surfactant-free solution a circulation pattern can be observed inside the forming drop at the first propagation step while on the sides the dispersed phase velocity has large values (**Figure 11a**). The recirculation pattern shows that the droplet grows mainly in the radial direction during the the first propagation step while the continuous phase obstructs the growth of the droplet. As the droplet enters into the main channel, the circulation area moves gradually forward and weakens while the velocities increase (**Figure 11b**). These observations also agree with the results by Timgren et al. (2008) who studied the velocity fields inside and outside of a forming oil drop in a cross-flow rectangular channel using PIV. In addition, the aqueous solution is mainly transported to the tip via the sides of the droplet as the middle part moves at low velocity.
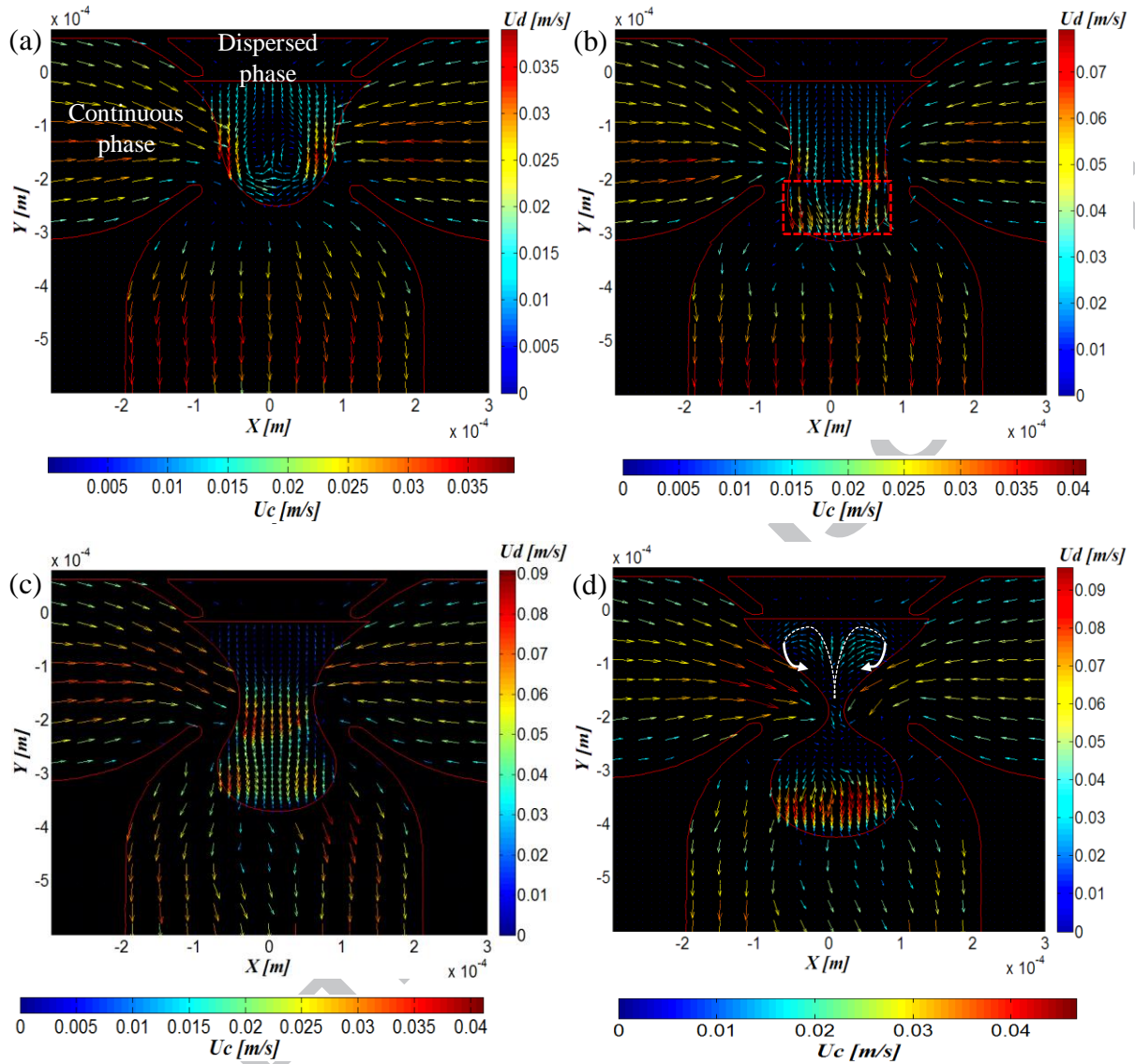
24

Figure 11: Averaged total velocity fields inside and outside the forming surfactant-free droplet. $Q_d = 0.01$ cm^3/min and $Q_c = 0.08$cm^3/min. Droplet diameter is equal to 203 μm. Images (a), (b), (c) and (d) correspond to propagation steps 1, 3, 5 and 7 respectively. Inset: Dotted rectangle indicates the region used to average the velocity profiles at the top of the droplet.

Under constant dispersed phase flowrate, the forming drop expands into the main channel and obstructs the flow of the continuous phase that has to travel through a smaller cross-sectional area next to the wall. As a result, the velocity and the pressure inside the continuous phase, at the cross-junction area, increase leading to the change in the neck curvature and to

the necking regime (**Figure 11c**). During the pinching–off stage (**Figure 11d**) the velocity acquires large values at the top part of the droplet.
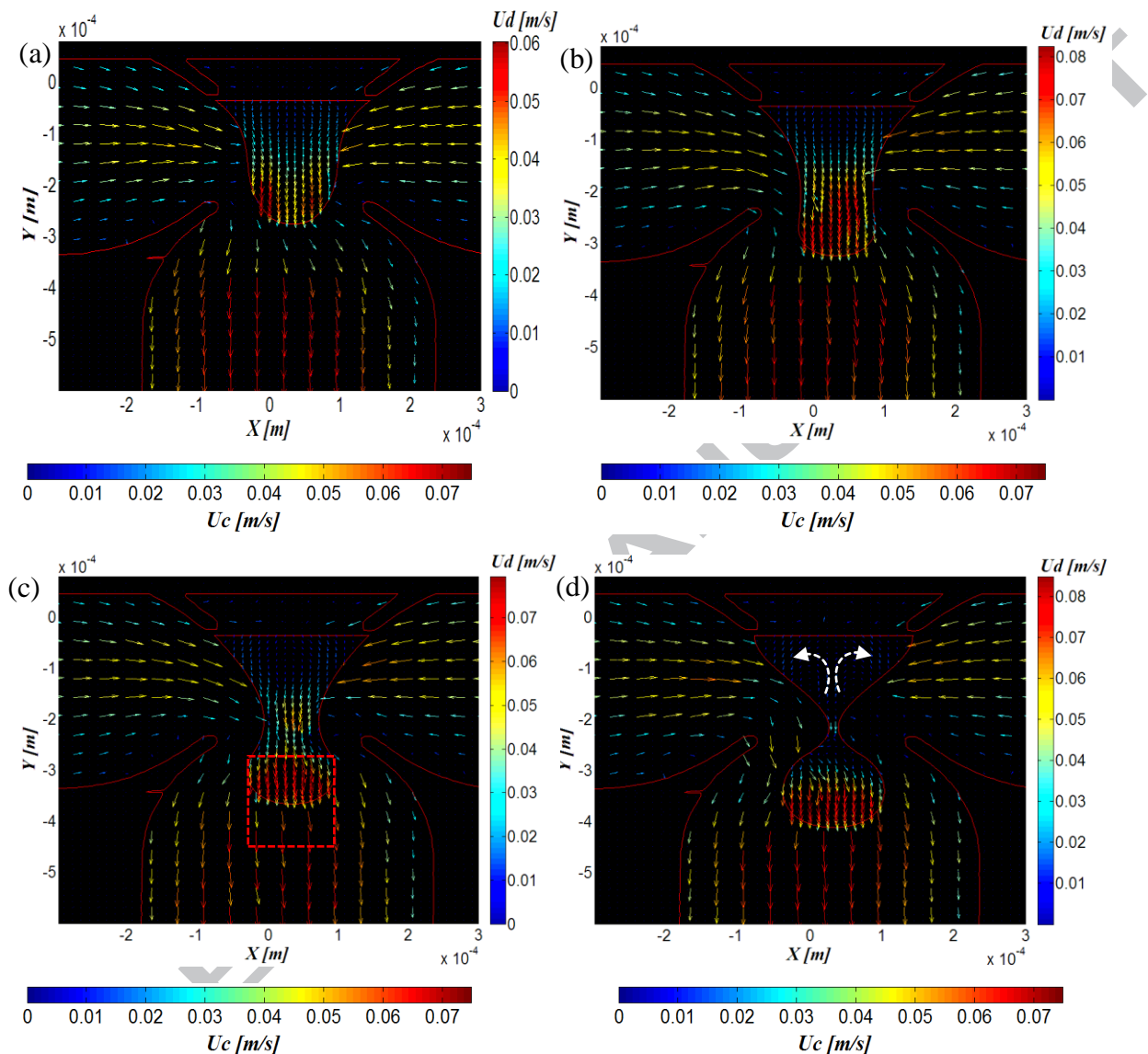

Figure 12: Averaged total velocity fields inside and outside the forming $C_{12}TAB$ droplet. Q_d = 0.01 cm³/min and Q_c = 0.08 cm³/min. Droplet diameter is equal to 142 μm. Images (a), (b), (c) and (d) correspond to propagation steps 1, 3, 5 and 7 respectively. Inset: Dotted rectangle indicates the region where the velocity difference between the two phases was calculated.

As the neck width reduces at a fast rate a flow inversion at the neck can be observed leading to a weak recirculation at the base of the droplet. It appears that the neck is stretched over two opposite directions (in the main channel by the continuous phase and towards the inlet by the flow reversal in the dispersed phase) that lead eventually to the neck break up.

Once the drop has detached, the dispersed phase pulls back into its inlet channel under the action of surface tension.

During the formation of the C_{12}TAB droplet (**Figure 12**), a recirculation pattern cannot be observed during the expansion stage (**Figure 12a**). As the droplet moves into the main channel, the velocity is more uniform and acquires larger values at the top part of the droplet (V ~ 0.076 m/s) (**Figure 12b**) compared to the surfactant-free case (V ~ 0.065 m/s) in **Figure 11b.** The differences of the C_{12}TAB system compared to the pure one can be attributed to the accumulation of surfactant to the tip of the droplet from the flow of the continuous phase. The variations of surfactant concentration along the drop interface would initiate Marangoni effects which will cause the movement of the interface to the opposite direction. This motion may prevent the recirculation inside the drop; in addition the local accumulation of the surfactant would increase the rigidity of the interface and reduce any velocity gradients inside the drop. Riaud et al. (2018) who studied both numerically and experimentally the dynamics of surfactants during drop formation in a T-junction, found similar results at the expansion stage. The authors suggested that the accumulation of surfactants at the tip of the drop prevents recirculation inside the dispersed phase, makes the interface more rigid and leads to a more uniform velocity field compared to the surfactant-free case.

Figure 13 presents this difference in the averaged axial velocity profiles at the top part of the droplet (see Inset, Figure 11) between the surfactant-free and C_{12}TAB systems for the propagation steps 1 and 3 (that correspond to **Figures11a**, **11b**, **12a** and **12b** respectively). As can be seen during the first propagation step (step 1) the highest velocity values are at the side of the droplet whereas the lowest values are in the middle, which show that the dispersed fluid is mainly transported through the sides of the droplet. As the C_{12}TAB drop enters into the main channel (step 3), high velocities appear in the top part of the droplet whereas in the

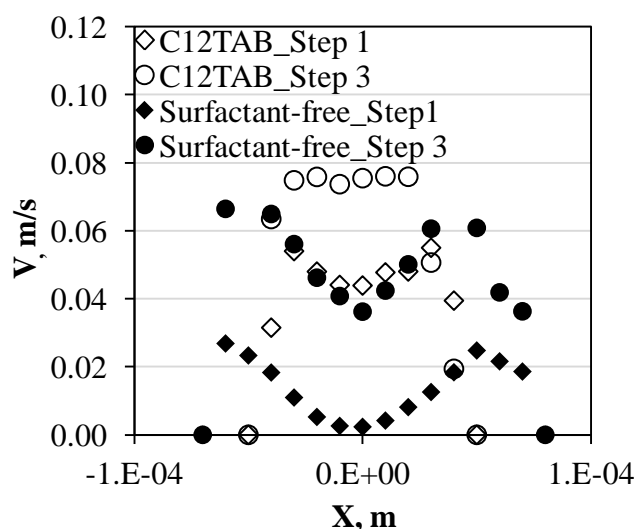surfactant-free system the highest velocities can still be seen at the sides of the droplet (**Figure 13**).

Figure 13: Averaged axial velocity profiles at the top part of the droplet for the surfactant-free and the C_{12}TAB solutions. C_{12}TAB_step 1, C_{12}TAB_step 3 and surfactant-free_Step 1, surfactant-free_Step 3 correspond to **Figures11a**, **11b**, **12a** and **12b** respectively.

At the next propagation steps (during necking and pinch-off stage) the highest velocities are in the middle of the C_{12}TAB droplet. This is different from the work by Carrier et al. (2015) who showed that during the growth of the droplet into the channel a weak recirculation pattern forms inside the newly forming droplet (aqueous SDS solution). They found the same recirculation pattern at the necking stage where the dispersed fluid is still transported to the tip via the sides of the droplet. As can been seen in **Figure 13**, in the surfactant-free system high velocities can be still found at the sides of the droplet at the necking stage and only at the pinch-off stage the highest velocities appear along the tip.

The necking stage of the C_{12}TAB droplet (**Figure 12c**) can be identified by an increase in the aqueous phase velocity in the neck region. The velocity vectors in the organic phase in **Figure 12c** are almost perpendicular to the aqueous/oil interface at the cross-junction inlet (similar to the surfactant-free case) leading to the thinning of the neck. At this stage, the local velocity difference at the top of the droplet between the two phases (see Inset, **Figure 12c**) is

28

larger (u_d = 0.045 m/s; u_c = 0.022 m/s) than in the surfactant-free solution (u_d = 0.071 m/s; u_c = 0.056 m/s) (**Figure 11**). During the pinching–off stage (**Figure 12d**) a less intense recirculation pattern, compared to the one in the surfactant-free case, can be observed at the base of the droplet. Carrier et al. (2015) who studied the formation of SDS droplets in a flow-focusing channel also reported a flow inversion and weak recirculation at the base of the dispersed phase during the pinch off stage.

The evolution of the forces at the different steps of the drop formation can be seen in **Figures 14a** and **b** for the surfactant-free and the C_{12}TAB solutions respectively.
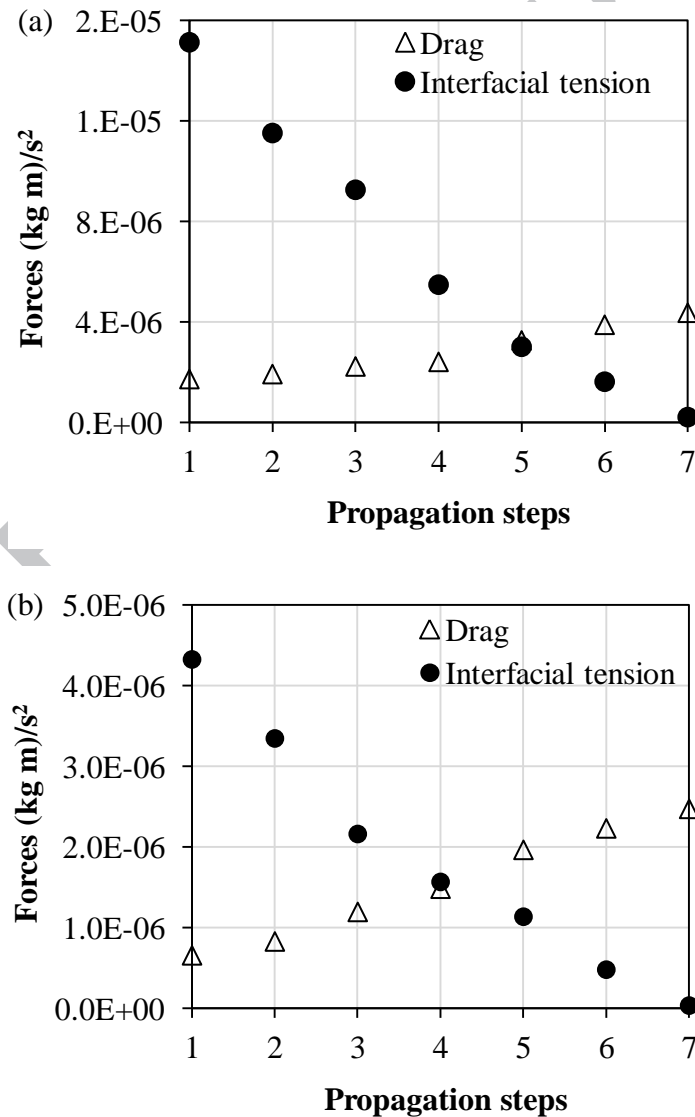

Figure 14: Forces during the formation of (a) surfactant-free and (b) C_{12}TAB surfactant-laden droplets. Q_D = 0.01 cm^3/min and Q_C = 0.08cm^3/min.

The forces were calculated based on **Eqs 1-2** using the data obtained from the experiments. The inertia force of the dispersed phase was found to be of the order of magnitude of $10^{-10} \frac{\text{kg} \cdot \text{m}}{\text{s}^2}$ and was not taken into account. As the droplet grows into the main channel, the difference in the local velocities between the continuous and the dispersed phases increases (**Figures 11 and 12**). This leads to an increase in the shear imposed by the continuous phase. At the same time, the pressure gradient in the continuous phase increases as the droplet size increases and blocks the flow-focusing inlet. As a result, the drag force gradually increases and overcomes the interfacial tension force at the propagation step 5 (**Figures 14a and b**). This is the step where the rate of the neck thinning changes as can be seen in **Figure 8** (for the experimental condition $Q_d = 0.01$ cm³/min and $Q_c = 0.08$ cm³/min) which denotes the transition from the expansion to the necking stage. The last points of the drag and interfacial tension forces that appear in **Figures 14a and b** correspond to pinch-off.

The axial velocity at the neck averaged over 40 PIV images is plotted in **Figure 15** at each propagation step for both fluid systems. As can be seen, the velocity increases until step 5 where it starts to decrease again until rupture occurs. In agreement with **Figures 11** and **12** the average velocity is higher for the surfactant-laden system, where there is no recirculation.
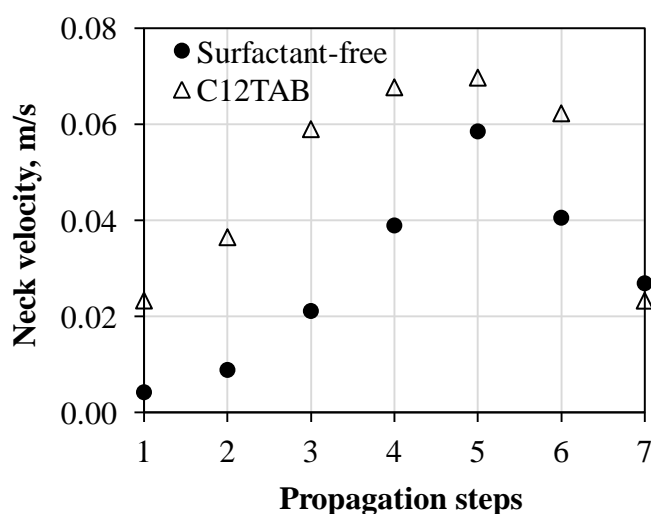

Figure 15: Averaged velocity at the neck obtained from PIV. $Q_d = 0.01$ cm³/min and $Q_c = 0.08$ cm³/min.

1.5 Conclusions

The flow patterns and drop formation process were studied in a flow focusing microfluidic device using silicone oil as the continuous phase and water/glycerol aqueous solutions that contained different concentrations of surfactants as the dispersed phase. An innovative two-colour Particle Image Velocimetry technique was used to obtain the flow fields in both phases and the characteristics of the forming drops.

It was found that the addition of surfactants reduced the areas of the squeezing and dripping regimes in a flow pattern map with the flowrates of the two phases as coordinates, whereas it extended the areas occupied by the threading and jetting regimes. The droplet formation process in the squeezing and dripping regimes was divided in three distinct stages, namely expansion, necking and pinch-off. The neck width reached at the end of the expansion and the necking stages was found to be depended on the continuous phase flowrates and on the type of surfactant. It was proposed that the dynamic interfacial tension of the different surfactant solutions, rather than the equilibrium one, explained the differences between the two surfactant systems. The rate of reduction of the neck width increased from the expansion to the necking stage. In general, the drops produced in the surfactant-laden solutions were smaller with higher tip curvature than in the surfactant free one. The velocity profiles in the squeezing regime showed that during the expansion stage, an internal circulation appeared at the center of the forming drop which gradually weakened as the droplet moved into the main channel. This circulation was less prominent in the surfactant-laden system which was attributed to the accumulaiton of surfactants at the drop tip. As the drop propagated into the main channel and the neck decreased in size, the velocities increased in the neck region. During pinching–off, a flow inversion at the thinnest part of the neck was observed which caused the dispersed phase to pull back into the inlet channel after the drop had detached. In general, the averaged velocity fields revealed that the addition of surfactants

increased the local velocity difference between the two phases compared to the surfactant-free case, for the same phase flowrates. Based on the geometric characteristics of the forming drops and the velocity fields obtained with PIV, the forces acting on the drop were estimated. It was found that drag forces overcome the surface tension ones between the expansion and the necking drop formation stages.

Future studies will investigate the process of droplet formation for different surfactant systems to understand the effects of interfacial tension and dynamics of surfactant absorption.

Acknowledgments

1.6 References

Anna, S., 2016. Droplets and Bubbles in Microfluidic Devices. Annu. Rev. Fluid Mech 48, 285–309.

Baret, J., Kleinschmidt, F., Harrak, A., Griffiths, A.D., 2009. Kinetic Aspects of Emulsion Stabilization by Surfactants: A Microfluidic Analysis. Langmuir 25, 6088–6093.

Carrier, O., Ergin, G., H Li, Watz, B., Funfschilling, D., 2015. Time-resolved mixing and flow-field measurements during droplet formation in a flow-focusing junction. J. Micromech. Microeng. 25.

Chen, X., Glawdel, T., Cui, N., Ren, C.L., 2015. Model of droplet generation in flow focusing generators operating in the squeezing regime. Microfluid Nanofluid 18, 1341–1353.

Chiarello, E., Gupta, A., Mistura, G., Sbragaglia, M., Pierno, M., 2017. Droplet breakup driven by shear thinning solutions in a microfluidic T-Junction. PHYSICAL REVIEW FLUIDS 2.

Chinaud, M., Roumpea, E., Angeli, P., 2015. Studies of plug formation in microchannel liquid–liquid flows using advanced particle image velocimetry techniques. Experimental Thermal and Fluid Science 69, 99–110.

Christopher, G., Noharuddin, N., Taylor, J., Anna, S., 2008. Experimental observations of the squeezing-to-dripping transition in T-shaped microfluidic junctions. PHYSICAL REVIEW E 78, 036317.

Cubaud, T., Mason, T.G., 2008. Capillary threads and viscous droplets in square microchannels. Physics of Fluids 20, 053302.

Fu, T., Ma, Y., Funfschilling, D., Li, H., 2009. Bubble formation and breakup mechanism in a microfluidic flow-focusing device. Chemical Engineering Science 64, 2392 -- 2400.

Fu, T., Ma, Y., Li, H., 2016. Breakup dynamics of slender droplet formation in shear-thinning fluids in flow-focusing devices. Chemical Engineering Science 144, 75–86.

Fu, T., Wu, Y., Ma, Y., Li, H.Z., 2012. Droplet formation and breakup dynamics in microfluidic flow-focusing devices: From dripping to jetting. Chemical Engineering Science 84, 207–217.

Funfschilling, D., Debas, H., Li, H.Z., Mason, T.G., 2009. Flow-field dynamics during droplet formation by dripping in hydrodynamic-focusing microfluidics. PHYSICAL REVIEW E 80, 015301.

Garstecki, P., Fuerstman, M., Stone, H., Whitesides, G., 2006. Formation of droplets and bubbles in a microfluidic T-junction—scaling and mechanism of break-up. Lab on a Chip 6, 437–446.

Garstecki, P., Stone, H., Whitesides, G., 2005. Mechanism for Flow-Rate Controlled Breakup in Confined Geometries: A Route to Monodisperse Emulsions. PHYSICAL REVIEW LETTERS 94, 164501.

Glawdel, T., Elbuken, C., Ren, C.L., 2012a. Droplet formation in microfluidic T-junction generators operating in the transitional regime. I. Experimental observations. PHYSICAL REVIEW E 85, 016322.

Glawdel, T., Elbuken, C., Ren, C.L., 2012b. Droplet formation in microfluidic T-junction generators operating in the transitional regime. II. Modeling. PHYSICAL REVIEW E 85, 016323.

Glawdel, T., Ren, C.L., 2012. Droplet formation in microfluidic T-junction generators operating in the transitional regime. III. Dynamic surfactant effects. PHYSICAL REVIEW E 86, 026308.

Graaf, S., Nisisako, T., Schroen, C., Sman, R., Boom, R., 2006. Lattice Boltzmann Simulations of Droplet Formation in a T-Shaped Microchannel. Langmuir 22, 4144-4152.

Husny, J., Cooper-White, J., 2006. The effect of elasticity on drop creation in T-shaped microchannels. J. Non-Newtonian Fluid Mech 137, 121−136.

Jin, F., Gupta, N.R., Stebe, K.J., 2006. The detachment of a viscous drop in a viscous solution in the presence of a soluble surfactant. PHYSICS OF FLUIDS 18, 022103.

Kovalchuk, N., Nowak, E., Simmons, M.J., 2016. Effect of Soluble Surfactants on the Kinetics of Thinning of Liquid Bridges during Drops Formation and on Size of Satellite Droplets. Langmuir 32, 5069−5077.

Kovalchuk, N.M., Roumpea, E., Nowak, E., Chinaud, M., Angeli, P., Simmons, M.J., 2018. Effect of surfactant on emulsification in microchannels. Chemical Engineering Science 176, 139−152.

Lee, W., Walker, L., Anna, S., 2009. Role of geometry and fluid properties in droplet and thread formation processes in planar flow focusing. PHYSICS OF FLUIDS 21, 032103.

Liu, H., Zhang, Y., 2011. Droplet formation in microfluidic cross-junctions. PHYSICS OF FLUIDS 23, 082101.

Riaud, A., Zhang, H., Wang, X., Wang, K., Luo, G., 2018. Numerical Study of Surfactant Dynamics during Emulsification in a T-Junction Microchannel. Langmuir 34, 4980-4990.

Seemann, R., Brinkmann, M., Pfohl, T., Herminghaus, S., 2012. Droplet based microfluidics Reports on Progress in Physics 75, 016601.

Steijn, V., Kreutzer, M.T., Kleijn, C.R., 2007. μ-PIV study of the formation of segmented flow in microfluidic T-junctions. Chemical Engineering Science 62, 7505 – 7514.

Timgren, A., Tragardh, G., Tragardh, C., 2008. Application of the PIV technique to measurements around and inside a forming drop in a liquid–liquid system. Exp Fluids 44, 565–575.

Utada, A.S., Fernandez-Nieves, A., Stone, H., Weitz, D., 2007. Dripping to Jetting Transitions in Coflowing Liquid Streams. PHYSICAL REVIEW LETTERS 99, 094502.

Wang, K., Lu, Y.C., Xu, J.H., Luo, G.S., 2009. Determination of Dynamic Interfacial Tension and Its Effect on Droplet Formation in the T-Shaped Microdispersion Process. Langmuir 25, 2153-2158.

Wong, V., Loizou, K., Lau, P., Graham, R.S., Hewakandamby, B.N., 2017. Numerical studies of shear-thinning droplet formation in a microfluidic T-junction using two-phase level-SET method. Chemical Engineering Science 174, 157–173.

Xu, J.H., Li, S.W., Tan, J., Luo, G.S., 2008. Correlations of droplet formation in T-junction microfluidic devices: from squeezing to dripping. Microfluid Nanofluid 5, 711–717.

Experimental study of droplet formation in a flow-focusing microchannel

Evangelia Roumpea, Nina M. Kovalchuk, Maxime Chinaud, Emilia Nowak,
Mark J.H. Simmons, Panagiota Angeli

Highlights

- Use of an innovative, two-colour micro-PIV technique to investigate velocity fields;

- Study of kinetics of surfactant absorption during the droplet formation process;

- Development of a mechanistic model for the droplet formation based on PIV data;

- Investigation of the effect of surfactants on the flow pattern maps

36